Study of Flow Control by Localized Volume Heating in Hypersonic Boundary Layers

By S. Kirilovskiy†, P. Polivanov†, A. Sidorenko†, A. Maslov†, M. Keller‡ AND M. J. Kloker‡

†Khristianovich Institute of Theoretical and Applied Mechanics (ITAM)
Russia 630090, Novosibirsk, Institutskaya str. 4/1
‡Institute for Aerodynamics und Gas Dynamics (IAG), University of Stuttgart
Pfaffenwaldring 21, 70569 Stuttgart, Germany

Boundary-layer flow control is a prerequisite for a safe and efficient operation of future hypersonic transport systems. Here, the influence of an electric discharge – modeled by a heat-source term in the energy equation – on laminar boundary-layer flows with zero pressure gradient at Mach 3, 5, and 7 is investigated numerically. The aim is to appraise the potential of electro-gasdynamic devices for an application as turbulence generators in the super- and hypersonic flow regime. The results with one or multiple localized heat-source elements are compared to cases with roughness elements serving as classical passive trips. The numerical simulations are performed using the commercial code ANSYS FLUENT (by ITAM) and the high-order finite-difference DNS code NS3D (by IAG), the latter allowing for the detailed analysis of laminar flow instability. For the investigated setups with steady heating transition to turbulence is not observed, due to the Reynolds-number lowering effect of heating. However, simulations with an unsteady heat source at adequate “roughness“ Reynolds number show the onset of transition.

1. Introduction

The methods of active and passive boundary-layer control may significantly improve the performance of prospective hypersonic transport systems. One of the critical problems of a hypersonic aircraft is the presence of separation zones arising as a result of an interaction between shock waves and boundary layers. The flow separation at hypersonic speed leads to a considerable increase of the dynamic and thermal load, and to a deterioration of the inlet flow, one possible cause for engine failure, see, e.g., [1]. The classical method for separation suppression is the application of vortex generators [2, 3]. Usually, vortex generators consist of three-dimensional wedges or a system of blowing jets. In an initially laminar flow, vortex / streak generators trigger transition to turbulence making the boundary layer more resistive to flow separation, and in turbulent flow they enhance mixing with the same effect. However, classical vortex generators result in high thermal loads making them difficult to use in real-flight applications, and – in case of blowing-jet systems – are technically complex.

Alternatively, plasma actuators can be used. Electro-gasdynamic devices are relatively easy to use, simple to integrate into the aircraft surface, and allow to induce high-frequency disturbances into the flow field. Depending on the flow regime the electric discharge may operate with varying power and frequency. The main impact of plasma action on the flow is a heat deposition. This results in the development of minor shock waves and the deformation of the boundary layer. Moreover, using diverse types of electric discharge like corona discharge or dielectric barrier discharge allow to create an ion wind in the boundary layer.

Today, the study of plasma-actuator effects on the flow behavior is unsystematic and patchy [4, 5]. This results in difficulties defining the scope of plasma vortex-generator applications. The existing experimental techniques do not permit to perform a detailed study of the boundary-layer structure under the influence of an electric discharge. Besides, the systematic experimental investigation of plasma vortex generators requires significant financial resources. Numerical simulations however enable a detailed understanding at relatively low financial costs.

It is assumed that an electric discharge primarily generates a significant local energy deposition. The comparison of experimental and numerical data [6] shows that an electric discharge can be simulated quite well by using a region of heat deposition and volumetric force in the Navier-Stokes equations, the latter being of minor importance for localized hot discharges. In the following, the effects of an electric discharge on laminar super- and hypersonic boundary-layer flows are investigated numerically. To this end, simulations are performed using the commercial flow solver ANSYS FLUENT applied by ITAM, and the IAG in-house high-order code NS3D applied by IAG.

2. Setup and Flow Parameters

The goal of this work is to investigate and compare the influence of (i) localized solid roughness and electric-discharge elements on laminar boundary-layer flows, and (ii) of solid cylinders and cylindrical discharge elements in the free stream of the flow at Mach numbers 3, 5, and 7 with zero streamwise pressure gradient. In order to model hot-plasma applications a (steady) heat-source term W is added to the right-hand side of the energy equation. This is in contrast to cold-plasma applications, where a volume-force term is considered in the momentum equations.

In the first part, a localized heating element located near the surface within the boundary-layer flow is considered. The results are compared to simulations with a solid roughness element. Both two- and three-dimensional simulations of a quadratic and cubic element, respectively, are performed. The flow parameters are based on a fixed total temperature $T_0 = 800\ K$, wall temperature $T_w = 300\ K$, and a reference dynamic pressure $\rho_\infty u_\infty^2/2 = 53375\ Pa$ in order to have energetically similar flows. Also, wind-tunnel facilities on hand can be operated at these parameters for future experimental investigations. An overview of the simulation-setup parameters is given in Tab. 1. For a single three-dimensional roughness element, results comparable for different settings are expected for

$$Re_{kk} = \frac{\rho_k u_k k}{\mu_k} = const.\ , \tag{2.1}$$

where ρ_k is the density, μ_k represents the viscosity, u_k indicates the velocity at the height of the roughness in the undisturbed boundary layer, and $k\ (= 0.2\ mm)$ is the element height of both the quadratic/cubic roughness or heating. The element positions x_0 for different Mach-number flows are chosen such that $Re_{kk} = 244$, being a near-critical value, i.e. laminar-turbulent transition may be influenced by the roughness. This value has been chosen in a first step for a fundamental comparison of the effects of a roughness- and heating-element. Tab. 2 contains an overview of the element locations, and the respective boundary-layer parameters. In order to obtain an equivalent heating impact for

M_∞	$p_\infty,\ Pa$	$T_\infty,\ K$	Re_{unit}	$u_\infty,\ m/s$
3	8472	285.8	$5.9 \cdot 10^6$	1017
5	3050	133.4	$10.0 \cdot 10^6$	1158
7	1556.1	74.1	$17.5 \cdot 10^6$	1208

TABLE 1. Simulation parameters.

M_∞	$x_0,\ m$	$\delta,\ mm$	$\delta^*,\ mm$	$\Theta,\ mm$	k/δ	$R_{x_0} = \sqrt{Re_{x_0}}$	$W_0,\ W/m^3$
3	0.1830	1.0596	0.4950	0.1160	0.1888	1039	$3.25 \cdot 10^{11}$
5	0.0206	0.4441	0.3000	0.0296	0.4503	454	$3.70 \cdot 10^{11}$
7	0.0077	0.3230	0.2569	0.0136	0.6192	368	$3.86 \cdot 10^{11}$

TABLE 2. Boundary-layer parameters at the position of the roughness or heating element x_0.

all three Mach numbers the volume and relative power density applied is kept constant. The power density of the heating element (W) is compared to the enthalpy power of the free-stream flow (W_0) in a crosscut with area k^2, divided by the element volume k^3:

$$W_0 = c_p T_0 \cdot \frac{\rho_\infty u_\infty}{k}\ , \tag{2.2}$$

with c_p being the specific heat and T_0 the total temperature. For its values see Tab. 2, and mostly $W/W_0 = 0.27$ has been applied.

The paper is organized as follows: Sec. 3 presents the numerical methods, and Sec. 4 the comparison of the results in a test case at Mach 5 obtained by FLUENT and NS3D. In Sec. 5 investigations on the laminar-instability alteration using NS3D with a controlled disturbance input are discussed. Sec. 6 deals with investigations at Mach numbers 3, 5, and 7, at a higher $Re_{kk} = 3400$, and in Sec. 7 a comparison between the effects of a solid cylinder and a cylindrical discharge in the free stream is performed. Finally, Sec. 8 summarizes the main findings and contains some concluding remarks.

3. Numerical Methods

Simulation results for a Mach 5 boundary-layer flow obtained using FLUENT are compared to corresponding time-accurate numerical simulations obtained by the 6^{th}-order finite-difference code NS3D. Both codes solve the time-dependent three-dimensional compressible Navier-Stokes equations. Sutherland's law is used to calculate the dynamic viscosity as a function of temperature. In this first study on the effects of a heat source air is treated as a non-reacting calorically perfect gas with constant Prandtl number $Pr = 0.71$ and constant specific-heat ratio $\gamma = 1.4$. Thus the temperature within the heated volume attains higher values than with thermochemical effects included. However it is expected that the temperature and velocity values downstream the element are not much affected.

3.1. *FLUENT Code*

ANSYS FLUENT [7] is based on a second-order finite-volume method for the discretization in space. The time integration is done either by means of an explicit 4-stage Runge-Kutta scheme or a second-order dual-time-stepping method for the implicit formulation.

3.2. *NS3D Code*

The NS3D code solves the time-dependent three-dimensional compressible Navier-Stokes equations in non-dimensional form. The fundamentals of the algorithm can be found in [8–11]. Sub-domain compact finite differences of 6^{th}-order are used for the spatial discretization in streamwise and wall-normal direction [12,13]. For three-dimensional simulations the derivatives in spanwise direction are computed by means of a Fourier-spectral discretization, due to the assumed periodicity of the flow field. The classical explicit 4^{th}-order Runge-Kutta procedure is applied for the integration in time. The code uses a hybrid parallelization of both MPI for domain decomposition in streamwise and wall-normal direction, and OpenMP for the spanwise direction. The electric discharge is modeled by a steady heat-source term W in the energy equation. The code allows for a reliable detection of any enhanced laminar-flow instability leading to self-excited unsteadiness in case, e.g. by grown numerical background noise. Note that the pressure rise across the emanating shock is not severe and shock capturing techniques are not required for the present simulations.

3.3. *Computational Domain, Boundary Conditions and Initial Condition*

For the test-case simulations presented in Sect. 4 we consider a hypersonic laminar boundary-layer flow over a flat plate with zero pressure gradient at a free-stream Mach number of $M_\infty = 5$. According to Tab. 1 the free-stream temperature and pressure are given by $T_\infty = 133.4\ K$ and $p_\infty = 3050\ Pa$, respectively. A FLUENT precursor simulation of a flat-plate boundary-layer flow without heat source serves as an initial condition. The flow variables prescribed at the inflow ($x = 0.016\ m$) are fixed. Note that the origin of the coordinate system is placed at the leading edge of the flat plate. At the outflow ($x = 0.025\ m$) the governing equations are solved neglecting the second-x-derivative terms. At the wall the no-slip, no-penetration boundary conditions are imposed on the velocity components. The pressure is calculated according to $\partial p/\partial y|_w = 0$, the density from the equation of state, and the temperature is set to $T_w = 300\ K$. At the free-stream boundary ($y = 0.002\ m$), all flow variables are computed such that the gradient along spatial characteristics is zero, except for the pressure, which is computed from the equation of state. In wall-normal direction the computational domain extends to a height of $y_M \approx 4.5\ \delta_0$, where $\delta_0 = 0.4441\ mm$ is the laminar boundary-layer thickness at the position of the heat source, based on $U/U_\infty = 0.99$. The grid is equidistant in streamwise and wall-normal direction. If not stated otherwise, the grid resolution in streamwise and wall-normal direction is equal to the grid resolution of the FLUENT simulations in the region of the heat source, $\Delta x = 0.0222\ mm$ and $\Delta y = 0.00555\ mm$. For the three-dimensional validation simulations the spanwise extent of the computational domain is set to $\lambda_z = 3 \cdot \delta_0 = 0.00133\ m$ with $\Delta z_{NS3D} = 0.0208\ mm$ ($\Delta z_{FLUENT} = 0.0333\ mm$). Since FLUENT offers an implicit time integration, the time step of the explicit Runge-Kutta scheme has to be approximately forty times smaller, $\Delta t = 1.3 \cdot 10^{-10}\ s$. The front of the heat source with side length $k = 0.2\ mm \approx 0.5\delta_0$ is located at $x = 0.02\ m$. A 5^{th}-order polynomial is used for a smooth ramping at the edges. The ramping region has a length of $0.2k$ (cf. inset of Fig 1a). This is in contrast to the simulations with FLUENT, where no heat-source

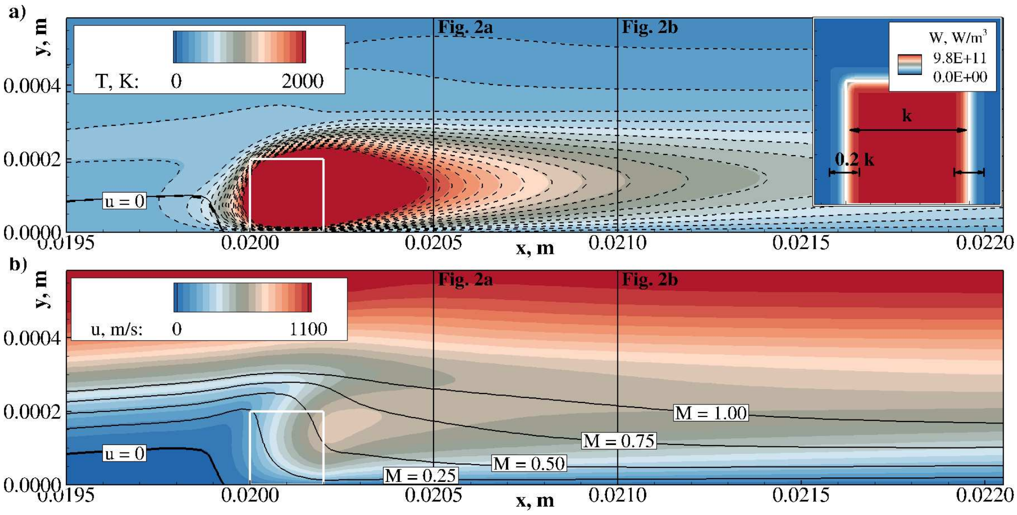

FIGURE 1. a) Isocontours of constant temperature and isolines of $u = 0$. FLUENT results are dashed, the heat-source extent is indicated by the white square. The inset shows the power-density distribution of the heat-source element. b) Isocontours of the u-velocity and isolines of the Mach number ($0.25 \leq M \leq 1.00$, $\Delta M = 0.25$). $W = 0.27 W_0$, $M_\infty = 5$.

ramping is used. The heat source has a power density of $W = 0.27\ W_0 = 9.8\ 10^{11}\ W/m^3$. The present simulations are carried out on block-structured Cartesian grids and are performed on the CRAY-XE6 system (AMD Opteron(tm) 6276 Interlagos @ 2.3 GHz) or the recently installed CRAY-XC30 test system (Intel SandyBridge @ 2.6 GHz) at the Federal High Performance Computing Center in Stuttgart (HLRS). For a three-dimensional simulation with e.g. $320(x) \times 120(y) \times 33(z) \approx 1.27 \cdot 10^6$ grid points the XC30-test system is roughly twenty-five percent faster. In this example, the domain is distributed on $8(x) \times 4(y)$ MPI tasks using 8 OpenMP threads in spanwise direction.

4. Test Case: FLUENT vs. NS3D

Figs. 1 and 2 show a comparison of the FLUENT and NS3D results for a two-dimensional simulation with quadratic heat source. The agreement is very good. Note that NS3D uses a 6^{th}-order spatial-discretization scheme and hence the grid resolution in streamwise and wall-normal direction can be reduced by a factor of two and four, respectively, leading to the same results as indicated by the blue lines in Figs. 2a,b. The localized heat source leads to an upstream recirculation region with a length of roughly $8k$. The u-velocity distribution downstream of the heat source, e.g., at $x = 0.0205\ m$ depicted in Figs. 1b and 2 shows a strong flow acceleration, resembling a wall-jet like profile with multiple generalized inflection points $(\rho(u'))' = 0$, with $' = d/dy$, in the near-field downstream. Note that the Mach number at a given height in the boundary layer increases due to the flow acceleration: The acceleration is stronger than the increase of the speed of sound by the heating.

The additional (large) heat-source term results in a significant sharpening of the time step limit, due to strong heat conductivity. Increasing the time step by a factor of four results in high DFL numbers, e.g. $DFL_y \approx 0.21$, without the source term considered. Then, the simulation is running near the viscous limit. However, the simulation does not crash and a wrong steady-state solution is obtained, see Fig. 3. The heat-source core

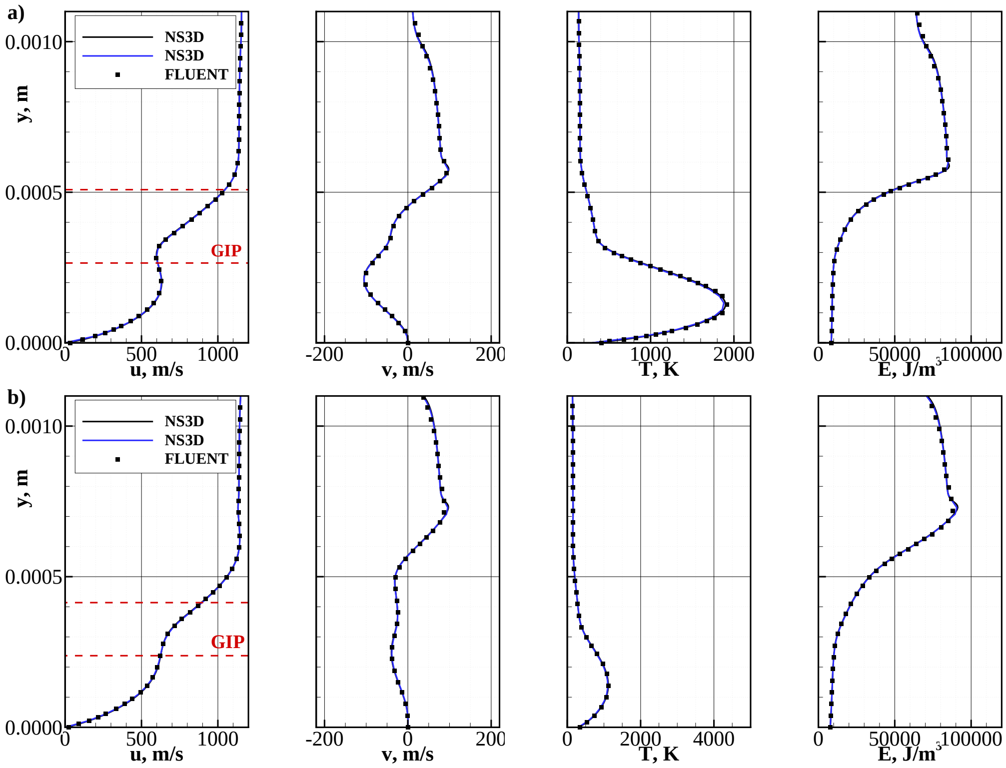

FIGURE 2. a,b) Velocity, temperature, and energy profiles at $x = 0.0205\ m$ and $x = 0.0210\ m$, respectively (cf. Fig. 1); the blue lines represent the results of the coarse grid with $\Delta x_{NS3D} = 2 \cdot \Delta x_{FLUENT}$ and $\Delta y_{NS3D} = 4 \cdot \Delta y_{FLUENT}$, black lines indicate results of identical grid resolution. $W = 0.27 W_0$, $M_\infty = 5$. The red dashed lines illustrate the y-position of the generalized inflection points.

temperature is much lower than for the convergence-proven reference case with four times smaller time step, see Figs. 1 and 2. Time-step-independence studies are thus imperative, also for steady-state solutions.

Good agreement is also observed for three-dimensional simulations with cubic heat source. A comparison of longitudinal and lateral crosscuts as well as several local profiles is shown in Fig. 4. Compared to the two-dimensional setup the upstream recirculation region is smaller, now approximately k long, and the core temperature is lower. As can be seen from Figs. 4b,c the downstream development of the u-velocity profile exhibits only very weak velocity streaks, if at all. The present flow significantly differs from the wake of a discrete roughness element, where strong wall-normal and spanwise gradients are observed for the streamwise velocity, see, e.g., [15, 16]. In contrast to a localized roughness element, the heat source leads to a characteristic flow lacking of notable vortices and streaks downstream. This is a consequence of the energy input acting similar to blowing through the leeward face of a roughness. For both two- and three-dimensional validation simulations a converged steady-state solution is attained and no self-excited unsteadiness is observed.

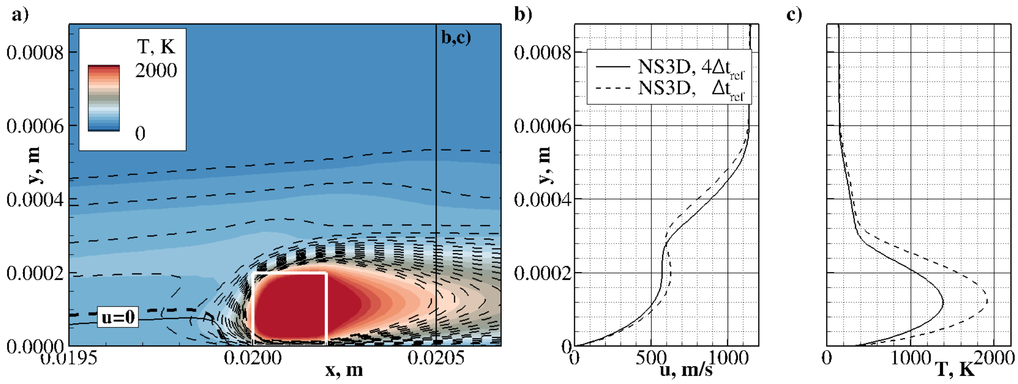

FIGURE 3. a) Isocontours of constant temperature and isolines of $u = 0$ for Δt_{ref} (– – – –) and $4\Delta t_{ref}$ (color). b,c) Velocity and temperature profiles at $x = 0.0205\ m$. Δt_{ref} is used for Figs. 1 and 2.

5. Instability Alteration Investigated by Controlled Unsteady Disturbance Input

All results discussed in this chapter were obtained using NS3D. The steady-state solution of the $M_\infty = 5$ flat-plate boundary-layer flow with cubic heat source described in Sec. 4 is used as a baseflow for investigations with controlled small-amplitude perturbation input. Two-dimensional disturbances in the frequency range $260\ kHz = U_\infty/(10{\cdot}\delta_0) \le f \le U_\infty/(2 \cdot \delta_0) = 1300\ kHz$ ($\Delta f = 260\ kHz$) are forced via localized blowing and suction at the wall upstream of the heat source. For the undisturbed baseflow the low frequency $f = U_\infty/(10 \cdot \delta_0)$ would be associated with first-mode disturbances, whereas the highest frequency $f = U_\infty/(2 \cdot \delta_0)$ would approximately correspond to typical second-mode disturbances. The perturbations are generated by means of a disturbance strip located at $x_{strip} = 0.0185\ m$ ($3\delta_0$ upstream of the heat source) using a disturbance amplitude of $A_{(v)} = 0.01$ and a streamwise disturbance-strip length of $l_{strip} = 0.4\ mm = 2k$. The disturbance function is given as $v(x^*) = -3 \cdot (2x^*)^4 + 4 \cdot (2x^*)^3$, for $x^* \in [0; 0.5]$, and $v(x^*) = -3 \cdot (2 - 2x^*)^4 + 4 \cdot (2 - 2x^*)^3$, for $x^* \in [0.5; 1]$, with $x^* = (x - x_{strip})/l_{strip}$. We point out that this study is based on a Fourier analysis of the forced unsteady flow for the investigation of the downstream development of the disturbances. An analysis by means of (BiGlobal) linear stability theory is not performed.

Figs. 5a,c illustrate the streamwise development of the maximum u-velocity perturbation (over y and z) for the cases with and without heat source, respectively. As shown in Fig. 5a all disturbances are neutral or damped. The presence of the cubic heat source gives rise to oblique (three-dimensional) disturbance waves. However, most of these modes rapidly decay immediately downstream of the heat source. The maximum amplitudes are located within the recirculation region upstream of the element. A weak amplification in the downstream region of the element is observed for the perturbation with frequency $f = U_\infty/(3.33 \cdot \delta_0) = 780\ kHz$. Instantaneous pressure fluctuations at the wall for the case with heat source are shown in Figs. 5e,f demonstrating that the initially two-dimensional disturbance waves become three-dimensional in the (near upstream) region of the heat source. This is also shown in Figs. 6 and 7 (cf. [15, 16]), where spanwise crosscuts of the u-velocity perturbations and the phase distribution of the pressure perturbations for all frequencies from $260\ kHz$ to $1300\ kHz$ are plotted at three locations downstream of the localized element. Second-mode behavior of

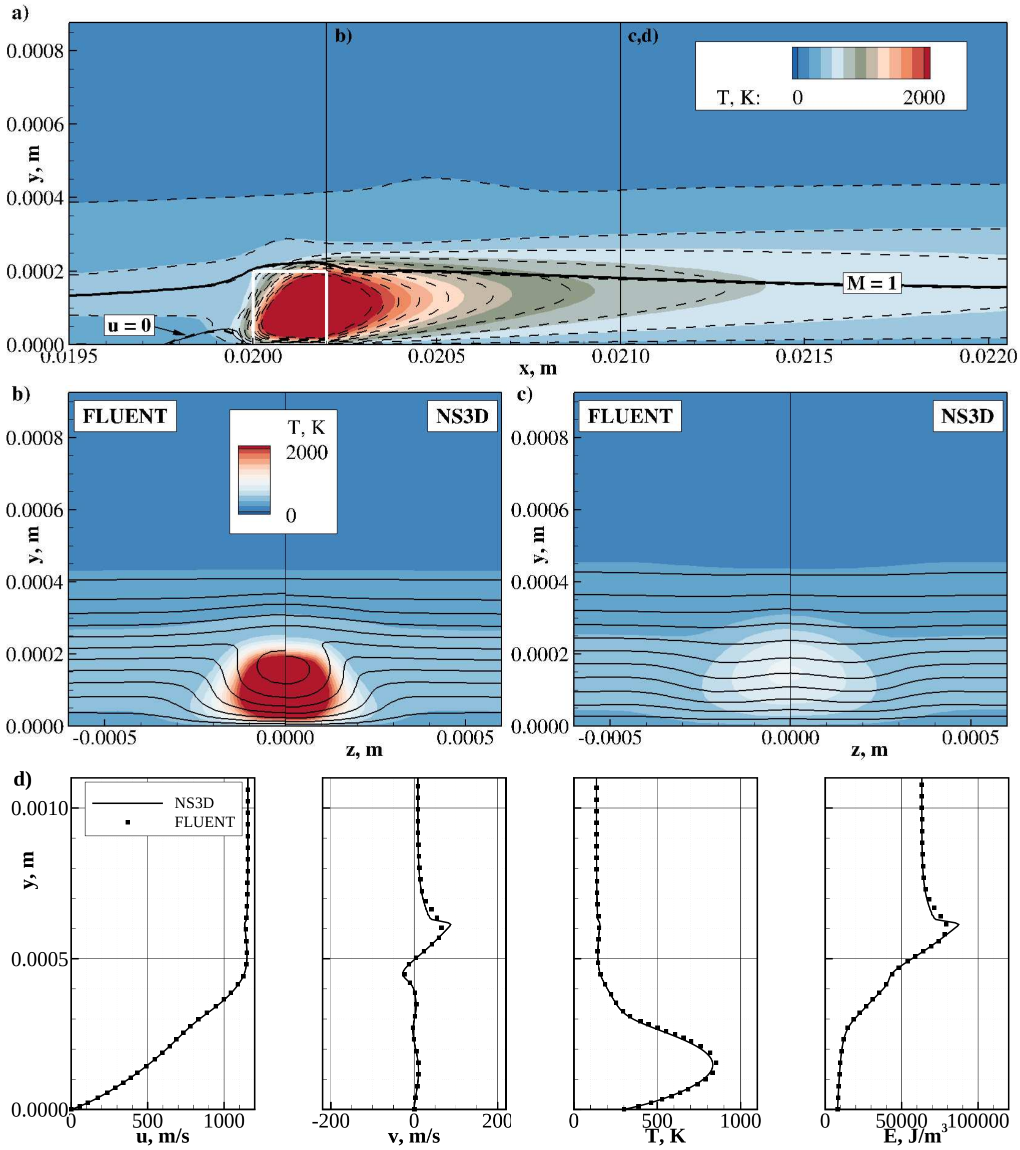

FIGURE 4. a) Isocontours of constant temperature and isolines of $u = 0$ and $M = 1$ along the centerline of the heat source ($z = 0.0\ m$). FLUENT results are dashed, the heat-source extent is indicated by the white square. b,c) Isocontours of constant temperature and isolines of constant u-velocity ($0\ m/s \leq u \leq 1200\ m/s$, $\Delta u = 100\ m/s$) in spanwise crosscuts at $x = 0.0202\ m$ and $x = 0.0210\ m$. d) Velocity, temperature, and energy profiles at $x = 0.0210\ m$ and $z = 0.0\ m$. $W = 0.27W_0$, $M_\infty = 5$.

the disturbances with frequency $1040\ kHz$ and $1300\ kHz$, albeit not that clear, is indicated by the phase change by π of the pressure perturbation along the wall-normal direction; this also holds for the dominating $780\ kHz$ disturbance. The wall cooling promotes the second mode which becomes three-dimensional due to the element. Note that the kinks of the high-frequency disturbances in the wake region of the heat source ($f = 1040\ kHz$ and $f = 1300\ kHz$ in Figs. 5a,b,c,d) are caused by competing modes hav-

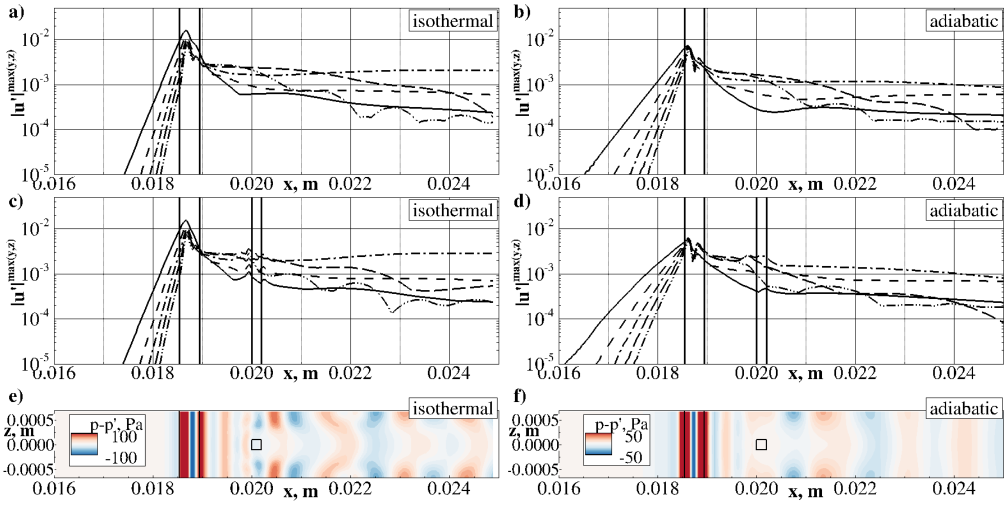

FIGURE 5. a,b,c,d) Downstream development of the maximum (over y and z) u-velocity perturbations ($260\ kHz$ (———), $520\ kHz$ (– – – –), $780\ kHz$ (—·—), $1040\ kHz$ (— — —), and $1300\ kHz$ (—··—)) for the cases with (c,d) and without (a,b) heat source using an isothermal (a,c) or adiabatic (b,d) wall boundary condition. e,f) Instantaneous pressure fluctuations ($p - p'$) at the wall for the cases with heat source (isothermal wall (e), adiabatic wall (f)). The locations of the disturbance strip and the cubic heat source are indicated by the black solid lines. $W = 0.27W_0$, $M_\infty = 5$.

ing the same frequency but slightly different wave numbers (beatings). This is illustrated by the u-velocity perturbations shown in Fig. 6. The shape of the perturbation with frequency $1040\ kHz$ at position $x = 0.022\ m$, for example, differs from the distribution shown at $x = 0.024\ m$ (Fig. 7).

In addition to the simulation with an isothermal, cool-wall boundary condition, an adiabatic wall ($T_{aw} \approx 700\ K$) is considered. All other parameters as described above are kept. The boundary-layer thickness increases to $\delta_{0,ad} = 0.635\ mm$ at $x = 0.02\ m$ without heat source. Upstream of the source no recirculation region develops for the three-dimensional setup. From a stability point of view, the adiabatic wall weakens the $780\ kHz$ disturbance (cf. Figs. 5a,c,e and Figs. 5b,d,f). For the cases with and without heat source all disturbances are neutral or damped. In contrast to the isothermal wall, a rather two-dimensional perturbation distribution is quickly restored in the near-downstream region of the heat source (Fig. 5f). In fact, the influence of the heat source on the instability is weaker, which likely can be explained by the smaller heat-source-extent to boundary-layer-thickness ratio: $k/\delta_{0,ad} \approx 0.3$, whereas $k/\delta_{0,is} \approx 0.5$.

6. Boundary-Layer Flow with 2-D and 3-D Roughness or Discharge Elements

All results discussed in this chapter were obtained using FLUENT. The wall-bounded shear-layer flow has been computed in two stages. First, a simulation of the whole flow field including the shock layer has been performed and the flow values (M, p, T, u, and v) in front of the (heating or roughness) element were stored. These values were used in subsequent simulations with or without element.

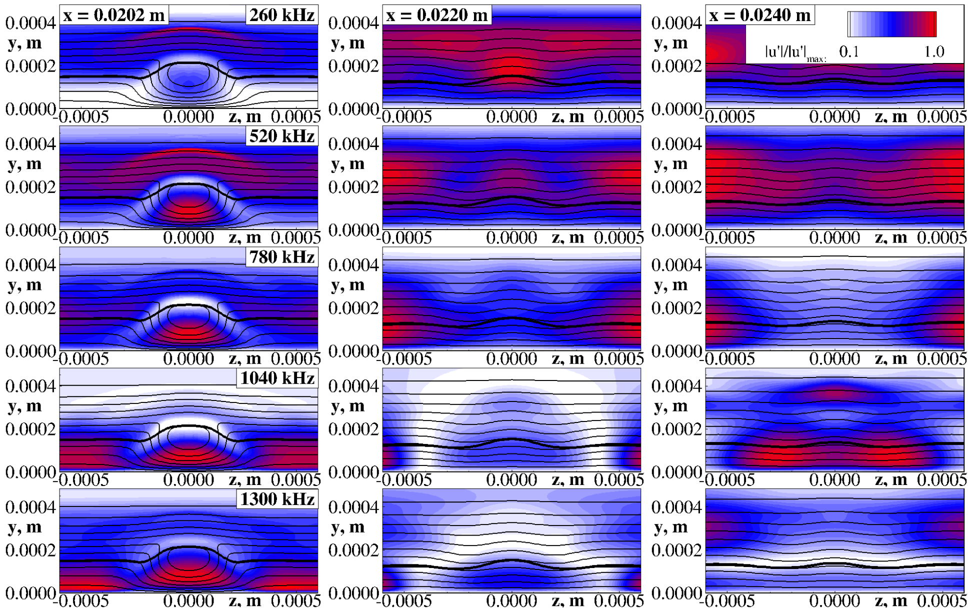

FIGURE 6. Colored isocontours of the normalized u-velocity perturbation ($|u'|/|u'|_{max}$) at the positions $x = 0.0202\ m$, $x = 0.0220\ m$, and $x = 0.0240\ m$ for the frequencies $260\ kHz$ to $1300\ kHz$. The thin solid lines represent the u-velocity distribution ($0\ m/s \leq u \leq 1200\ m/s$, $\Delta u = 100\ m/s$) of the unperturbed baseflow. The thick solid line indicates the sonic line $M = 1$. $W = 0.27W_0$, $M_\infty = 5$, isothermal wall.

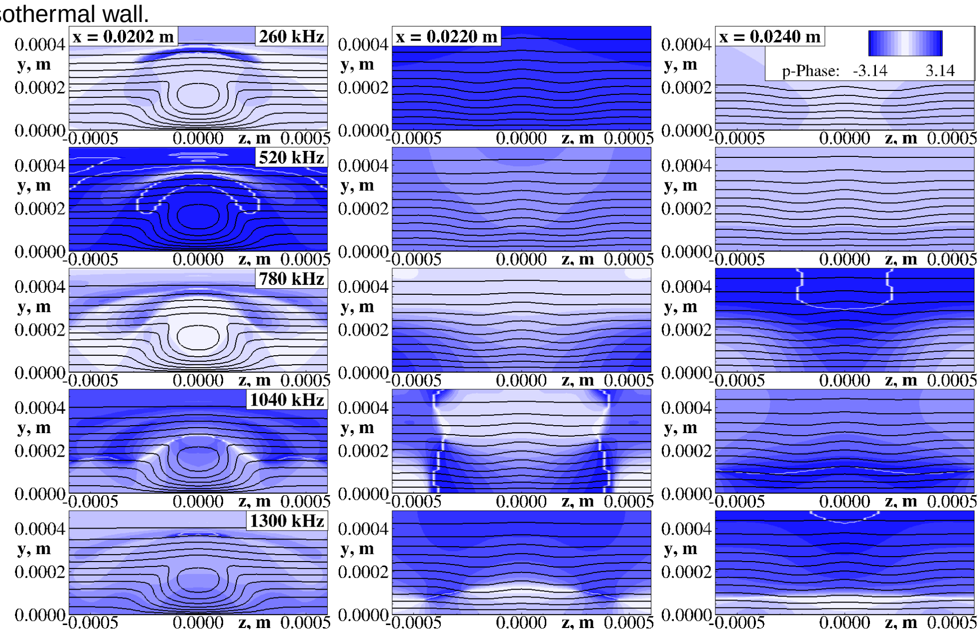

FIGURE 7. Colored isocontours of the p-perturbation phase at the positions $x = 0.0202\ m$, $x = 0.0220\ m$, and $x = 0.0240\ m$ for the frequencies $260\ kHz$ to $1300\ kHz$. The black solid lines represent the u-velocity distribution ($0\ m/s \leq u \leq 1200\ m/s$, $\Delta u = 100\ m/s$) of the unperturbed baseflow. $W = 0.27W_0$, $M_\infty = 5$, isothermal wall.

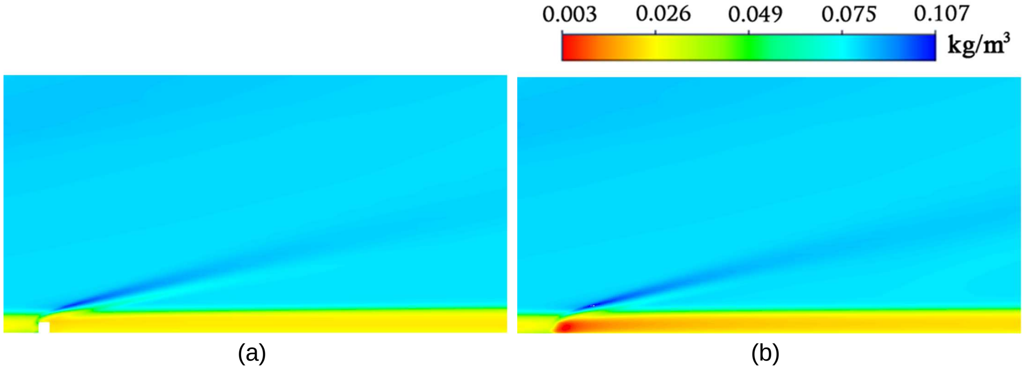

FIGURE 8. Density isocontours along the element centerline of a single 3-D roughness (a) and 3-D discharge (b). $M_\infty = 5$, $W = 0.27W_0$.

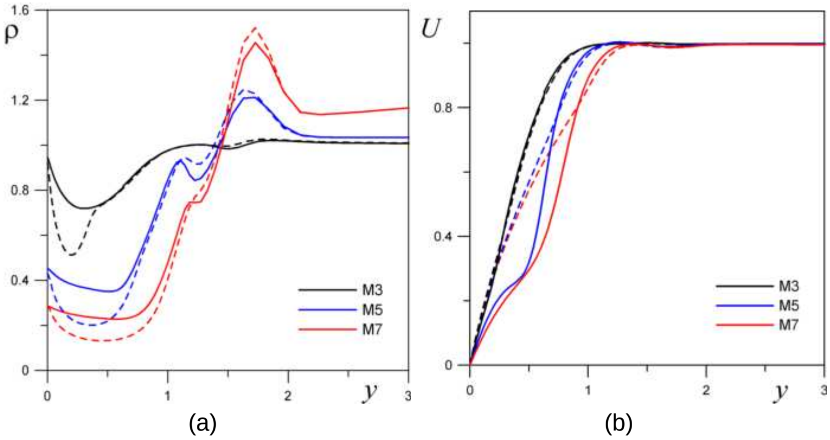

FIGURE 9. Dimensionless density (a) and velocity (b) profiles along the element centerline of a 3-D roughness (———) and 3-D discharge (– – – –) for $M_\infty = 3, 5, 7$. $W = 0.27W_0$; in section $M3 - x = 0.18639\ m$, $M5 - x = 0.02153\ m$, $M7 - x = 0.00887\ m$.

6.1. *Steady Cases*

In Fig. 8 density isolines for the flow with single 3-D roughness (Fig. 8a) or discharge (Fig. 8b) are demonstrated at $z = 0\ m$ for $M_\infty = 5$. Compression and expansion waves caused by the elements can be noticed.

In Fig. 9 density and velocity profiles are presented three boundary-layer thicknesses downstream a respective 3-D element. Values are non-dimensionalized by the free-stream density or the boundary-layer thickness, respectively. The density profiles for the two different types of elements are similar, indicating that we chose the flow parameters and heating power density correctly. The figures also demonstrate that the roughness element causes predominantly a velocity defect (solid lines in Fig. 9b), and the discharge a density defect (dashed lines in Fig. 9a).

In Fig. 10 a comparison between the 2-D and 3-D cases is presented for the density (a,b) and velocity (c,d) profiles for $M_\infty = 5$. From the density profiles it can be seen that in the 2-D cases the far-field waves are stronger than for the 3-D cases. The velocity-profile curvature in the 3-D roughness case is a consequence of the essentially three-

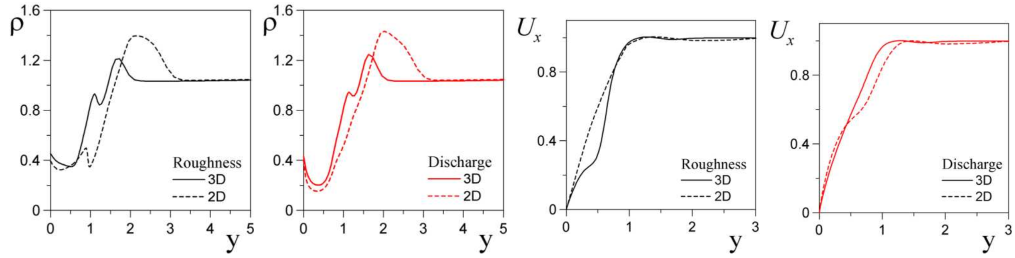

FIGURE 10. Dimensionless density (a,b) and velocity (c,d) profiles for single roughness (a,c) and discharge (b,d) at $M_\infty = 5$ of a 3-D case (———) and a 2-D case (– – – –). $W = 0.27W_0$; in section $M5 - x = 0.02153\ m$; $z = 0.0\ m$.

M_∞	$k,\ mm$	$surface,\ \%$	$flow,\ \%$
		2-D	
3	0.2	39	61
5	0.2	42	58
7	0.2	42	58
		3-D	
3	0.2	17	83
3	0.2477	16	84
5	0.2	61	39
7	0.2	45	55
7	0.1455	48	52

TABLE 3. Boundary-layer parameters.

dimensional flow around the roughness. The curvature of the velocity profile in the 2-D discharge case can be explained by higher heating in the 2-D case due to the difference in the effective form.

An analysis of the wall heat flux and the alteration of the flow parameters downstream of the heating reveals the ratio between the energy input into the flow and the wall. Tab. 3 shows this ratio for the 2-D and 3-D cases and the three investigated Mach numbers. In the 2-D cases the ratio is virtually constant unlike the 3-D cases. However, it remains also roughly constant for different characteristic lengths k at kept Mach number.

An analysis of the boundary-layer flow topology is presented in Fig. 11 by isosurfaces of the displacement thickness δ^* and momentum thickness Θ. It can be seen that δ^* increases, but Θ decreases over the local heating and the respective defect persists downstream.

Also simulations of single discharge elements with different volume were performed. In these simulations the ratio between k and the boundary-layer thickness was held constant as well as the power in the volume of heating, i.e. with changing k the power density is also changing. These simulations show that increasing k leads to increasing displacement thickness. Different volume of constant power heating leads to considerable differences in the boundary-layer parameters. All these data show that not only the power of heating is important for making the defect in the boundary layer but also the size of impact.

Looking at streamlines around and downstream the 3-D elements shows that steady

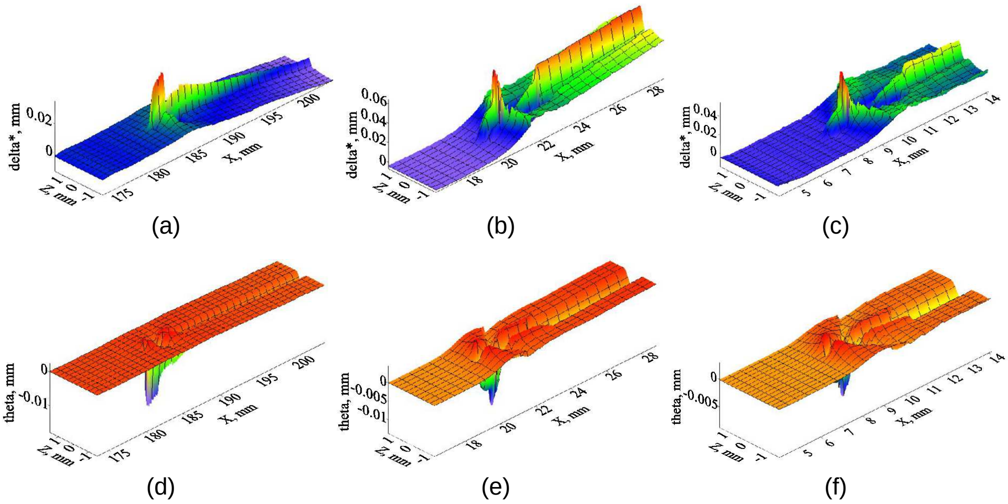

FIGURE 11. Isosurfaces of displacement (a,b,c) and momentum (d,e,f) thickness of boundary layers with heating for different Mach numbers. $W = 0.27W_0$, $k = 0.2\ mm$, $M_\infty = 3$ (a,d), $M_\infty = 5$ (b,e), $M_\infty = 7$ (c,f).

M_∞	3	x	$0.1\ mm$
p_∞	$16944\ Pa$	δ	$0.4039\ mm$
T_∞	$285.8\ K$	δ^*	$0.2440\ mm$
Re_{unit}	$1.18 \cdot 10^7$	Θ	$0.0551\ mm$
u_∞	$1017\ m/s$	Re_{kk}	3400
$\rho_\infty u_\infty^2$	$213495.4\ Pa$		

TABLE 4. Changed simulation parameters.

heating leads effectively to the formation of a kind of semi-infinite body in contrast to the effects of a roughness element, cf. Fig. 11.

6.2. *Unsteady Cases*

There is no (self-excited) laminar-turbulent transition in the previous cases. In order to reach the transitional stage the flow/turbulator configurations have been altered. The free-stream static pressure and Re_{kk} have both been increased by increasing k and the position of the element. Instead of one element now three staggered elements are used. Tab. 4 indicates the flow parameters. The height of the turbulator has been changed to $0.375\ mm$ and sizes in x- and z-direction (parallel to the wall) to $0.45\ mm$. Note that the "actual" Re_{kk} for the heated case is at least one order of magnitude lower than for a corresponding roughness, due to the decrease of density and the increase of viscosity by the heating.

In the case with three discharge elements steady and unsteady heating ($f = 80\ kHz$ and $240\ kHz$) was used. No onset of transition is observed for $f = 0\ kHz$ or $f = 80\ kHz$, but applying $f = 240\ kHz$ shows the start of the transition process. In Fig. 12 isosurfaces of the Q-criterion for roughness elements (a) and unsteady-heating elements with $f = 240\ kHz$ (b) are presented. With roughness elements the beginning of laminar-turbulent transition appears also near the end of the computational domain. These data show

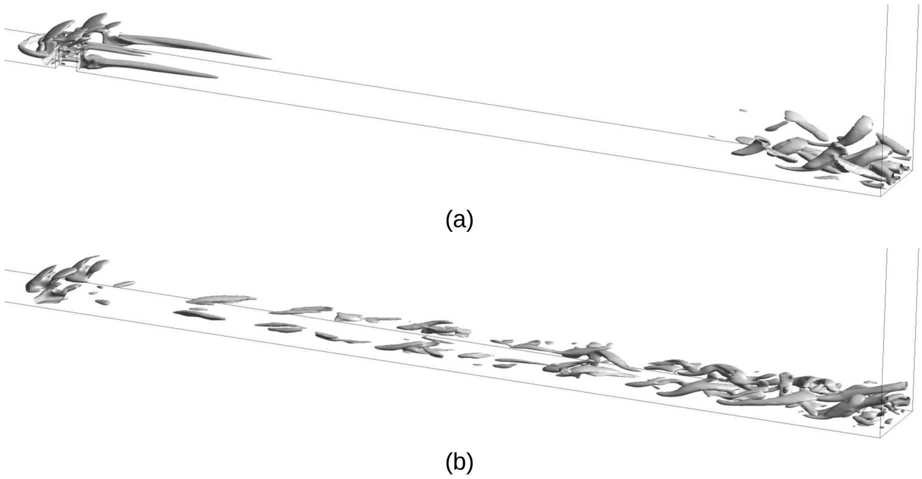

FIGURE 12. Isosurfaces of Q-criterion with roughness elements (a) and unsteady heating elements with $f = 240\ kHz$ (b). $W = 0.27W_0$, $M_\infty = 3$.

M_∞	$p_\infty,\ Pa$	$T_\infty,\ K$	Re_{unit}	Re_d
3	20000	285.8	$2.78 \cdot 10^4$	56
5	7150	133.4	$4.76 \cdot 10^4$	95
7	3650	74.1	$8.46 \cdot 10^4$	169

TABLE 5. Simulation parameters for flow over cylindrical body.

that only unsteady heating at adequate frequency can trigger turbulence like steady roughness can.

7. Free Shear Layers Downstream of a Transverse Cylinder or Cylindrical Heat Source

Laminar-turbulent transition in boundary layers cannot only be triggered by internal disturbances but also by turbulence in the free stream. To this end the feasibility of turbulence generation by a cylinder or cylindrical heat source in the free stream has been investigated. The ANSYS FLUENT package in 2-D formulation is employed for this study. Like before, the total temperature ($T_0 = 800\ K$) and a reference dynamic pressure ($\rho_\infty u_\infty^2/2 = 12500\ Pa$) were fixed. The flow parameters are specified in Tab. 5.

For these simulations the second-order method in space and fourth-order four-stage Runge-Kutta scheme in time were used. The computational domain is a rectangle area with C-type mesh. The diameter of the solid cylinder is $d = 2\ mm$. In Fig. 13 velocity isocontours are shown for the three Mach numbers. It can be seen that increasing the Mach number leads to a more stable flow, i.e. self-excited turbulence from background disturbances starts farther downstream at higher Mach numbers. Also it is observed that the recirculation zones for these cases have the same size, meaning that the flow parameters chosen for the comparison of the three different Mach numbers were chosen correctly.

The next step was setting a heating element instead of the solid cylinder and studying

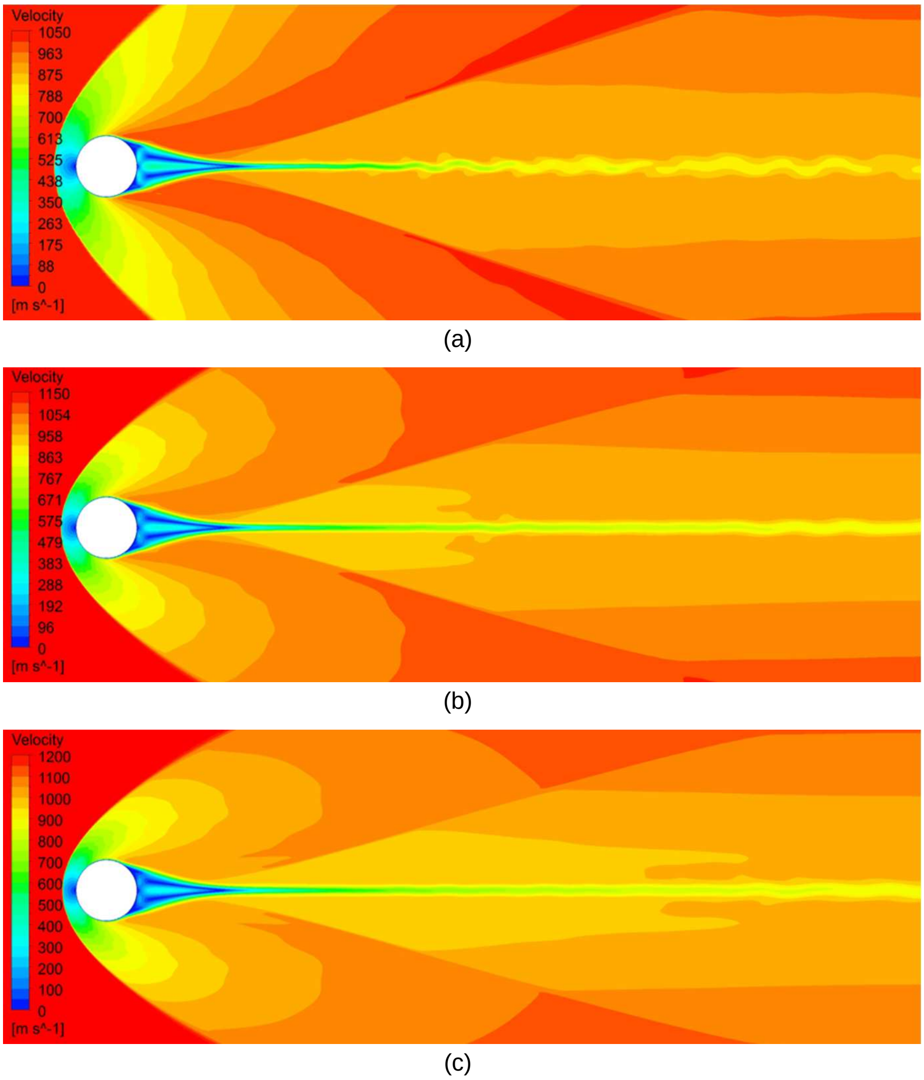

FIGURE 13. Velocity isocontours for the solid cylinder ($d = 2\ mm$) in the free-stream flow. $M_\infty = 3$ (a), $M_\infty = 5$ (b), $M_\infty = 7$ (c)

the flow downstream the heating. Investigations with varied power density have shown that increasing the power leads to an increase of the influence area, but the velocity gradients in the downstream trace did not change significantly. As in the case with steady heating in the boundary layer, a semi-infinite body appears in the free-stream flow (Fig. 14a) and no turbulence is observed. The use of three small discharge elements, each with size $0.3\ mm \times 0.04\ mm$ (Fig. 14b), exhibits a similar behavior. The generation of multiple shear layers apparently does not lead to laminar-turbulent transition either. The simulation with unsteady heating (Fig. 14c) shows that in the near wake each heating peak can be discerned, but downstream they average out in the far field and form also a kind of semi-infinite body. Compared to Fig. 14a a thinner, more concentrated high-speed streak develops due to the higher power density. Keep in mind

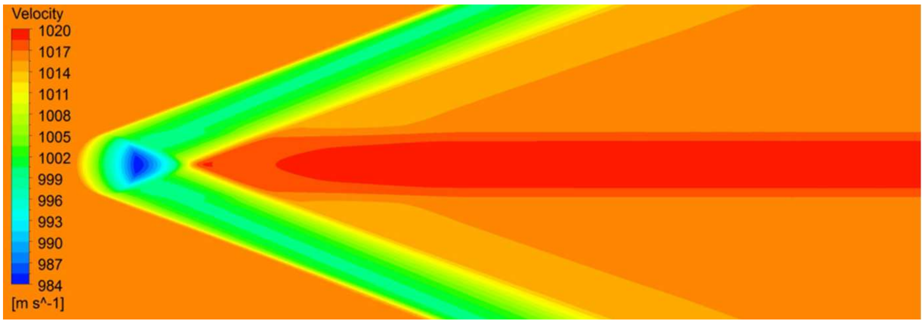

(a)

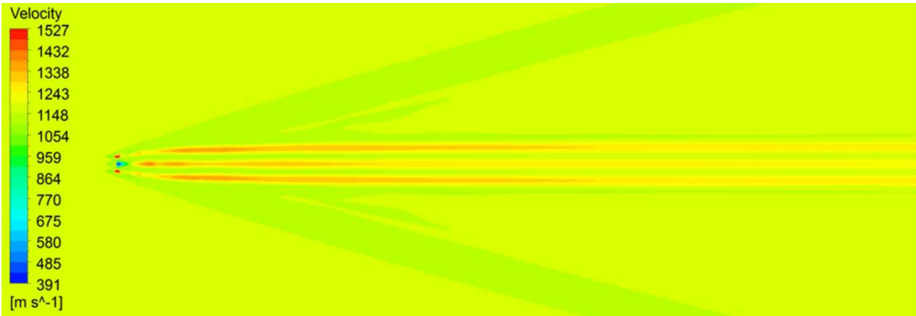

(b)

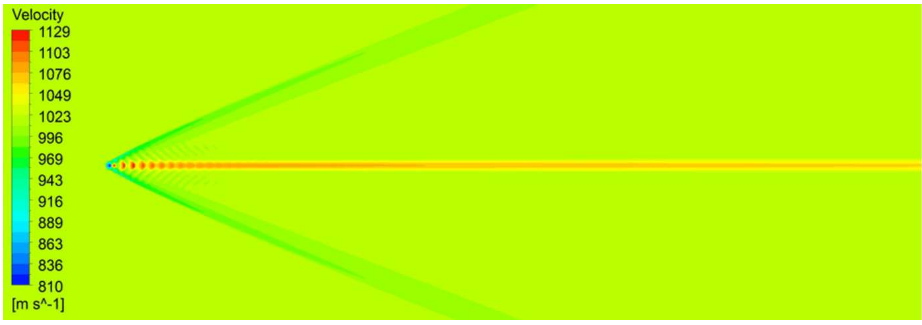

(c)

FIGURE 14. Velocity isocontours for the cases with one or multiple discharge elements in the free-stream flow. a) $M_\infty = 3$, $W/W_0 = 0.031$, $W = 10^{10}\ W/m^3$, one heating element with $d = 2\ mm$ (cf. d in Sects. 4-6). b) $M_\infty = 5$, $W/W_0 = 3.0$, $W = 1.1 \cdot 10^{12}\ W/m^3$, three rectangular heating elements with $0.3\ mm \times 0.04\ mm$ ($h = 0.24\ mm$). c) $M_\infty = 3$, $W/W_0 = 3.4$, $W = 1.1 \cdot 10^{12}\ W/m^3$, one unsteady heating element with $d = 0.2\ mm = 0.1 d_{ref}$.

that the integral power density of the unsteady heating is lower than for steady heating. For all three simulations the ratio $\left(\frac{W}{W_0}\frac{A}{A_{ref}}\right)$ is kept constant, with $A_{ref} = (\pi d^2)/4$ and $d = 2\ mm$.

8. Conclusions

The effects of an electric discharge, modeled by an additional heat-source term in the energy equation, on laminar boundary-layer flows at Mach 3, 5, and 7 are investigated by means of numerical simulations. The goal is to appraise the potential of electro-gasdynamic devices for an application as vortex generators / transition-triggering devices in a super- or hypersonic flow regime.

The simulations are performed using the commercial code ANSYS FLUENT applied by ITAM and the high-order DNS code IAG-NS3D applied by IAG, the latter allowing for the reliable detection of any enhanced laminar-flow instability. A comparison of the results gained by both codes shows a very good agreement for a test case, a Mach 5 boundary-layer flow with steady, two-dimensional or three-dimensional heat-source element. For these simulations at near-critical Re_{kk} a converged steady-state solution was attained and (self-excited) transition to turbulence could not be observed. The steady heating accelerates the flow strongly and effectively leads to the formation of a semi-infinite body. The three-dimensional mean-flow distortion is very weak compared to the effects of a roughness element. Moreover, the parameter Re_{kk} is significantly lowered by the decrease of density and the increase of viscosity due to the heating, despite the velocity increase. Note also that the additional (large) heat-source term results in a significant sharpening of the time step limit due to strong heat conductivity. Time-step-independence studies are thus imperative, also for steady-state solutions.

Simulations of a cubic heating element with forcing of controlled two-dimensional small-amplitude perturbations upstream of the element revealed mostly damped or neutral disturbance behavior for an adiabatic wall boundary condition, whereas for an isothermal, cool wall second-mode waves, forced to three-dimensionality by the heating element, undergo amplification downstream of the element. To trigger transition by localized volume-element heating, the corresponding (roughness) Re_{kk} must be increased by at least one order of magnitude, and be operated at an appropriate frequency.

Finally, two-dimensional simulations of shear layers after a solid cylinder were performed. It was demonstrated that an increasing Mach number leads to a more stable flow, i.e. transition to turbulence started farther downstream. No transition was triggered for corresponding cases with a steady or unsteady heat-source element in the free-stream flow.

Acknowledgments

This work was funded by the German Research Foundation (Deutsche Forschungsgemeinschaft) in the framework of the Collaborative Research Center SFB/TRR 40: Fundamental technologies for the development of future space-transport-system components under high thermal and mechanical loads, in which M.K and M.J.K. are involved. Computational resources were kindly provided by the Federal High Performance Computing Center Stuttgart (HLRS). Special thank goes to the organizing committee of the summer research program.

References

[1] BERRY, S. A., NOWAK, R. J. AND HORVATH, T. J. (2004). Boundary Layer Control for Hypersonic Airbreathing Vehicles. *34th AIAA Fluid Dynamics Conference, AIAA Paper 2004-2246*, Portland, OR, USA.

[2] LANSON, F. AND STOLLERY, J. L. (2006). Some Hypersonic Intake Studies. *Aeronautical J.*, **110**(1105), 145–156.

[3] LU, F. K., LI, Q., SHIH, Y., PIERCE, A. J. AND LIU, C. (2011). Review of Micro Vortex Generators in High-Speed Flow. *49th AIAA Aerospace Sciences Meeting, AIAA Paper 2011-31*, Orlando, FL, USA.

[4] KIMMEL, R. L., HAYES, J. R, CRAFTON, J. W., FONOV, S. D., MENART, J. AND SHANG, J. (2006). Surface Discharges for High-Speed Boundary Layer Control. *44th Aerospace Sciences Meeting, AIAA Paper 2006-0710*.

[5] IM, S., DO, H. AND CAPPELLI M. A. (2010). Dielectric Barrier Discharge Control of a Turbulent Boundary Layer in a Supersonic Flow. *Appl. Phys. Lett.*, **97**, 041503.

[6] BUDOVSKY, A. D. AND SIDORENKO, A. A. (2012). Numerical Simulation of Vortex Flow Control on a Cone at Incidence by Means of Electrical Discharge. *16th International Conference on the Methods of Aerophysical Research (ICMAR'2012), book of abstracts part 1*, 64–64, Kazan, Russia.

[7] ANSYS, INC. (2013). *www.ansys.com*.

[8] LINN, J. AND KLOKER, M. J. (2011). Effects of Wall-Temperature Conditions on Effusion Cooling in a Mach-2.67 Boundary Layer. *AIAA J.*, **49**(2), 299–307.

[9] KLOKER, M. J. (1998). A Robust High-Resolution Split-Type Compact FD Scheme for Spatial Direct Numerical Simulation of Boundary-Layer Transition. *Appl. Sci. Res.*, **59**, 353–377.

[10] BABUCKE, A., LINN, J., KLOKER, M. J. AND RIST, U. (2006). Direct Numerical Simulation of Shear Flow Phenomena on Parallel Vector Computers. In: Resch, M., Bönisch, T., Benkert, K., Bez, W., Furui, T. and Seo, Y. (Eds.): *High Performance Computing on Vector Systems*, 229–247.

[11] BABUCKE, A. (2009). *Direct Numerical Simulation of Noise Generation Mechanisms in the Mixing Layer of a Jet*. Ph.D. thesis, University of Stuttgart, Germany.

[12] KELLER M. AND KLOKER, M. J. (2013). Direct Numerical Simulations of Film Cooling in a Supersonic Boundary-Layer Flow on Massively-Parallel Supercomputers. In: Resch, M., Kovalenko, Y., Focht, E., Bez, W. and Kobaysahi, H. (Eds.): *Sustained Simulation Performance 2013* (accepted for publication).

[13] KELLER M. AND KLOKER, M. J. (2013). DNS of Effusion Cooling in a Supersonic Boundary-Layer Flow: Influence of Turbulence. *44th AIAA Thermophysics Conference, AIAA Paper 2013–2897*, San Diego, CA, USA.

[14] WHITE, F. M. (1991). *Viscous Fluid Flow*. McGraw-Hill.

[15] GROSKOPF, G., KLOKER, M. J. AND MARXEN, O. (2010). Bi-global Crossplane Stability Analysis of High-Speed Boundary-Layer Flows with Discrete Roughness. In: *Proceedings of the Seventh IUTAM Symposium on Laminar-Turbulent Transition 2009*, Stockholm, Sweden.

[16] GROSKOPF, G., KLOKER, M. J., STEPHANI, K. A., MARXEN, O. AND IACCARINO, G. (2010). Hypersonic Flows with Discrete Oblique Surface Roughness and Their Stability Properties. In: *Proceedings of the Summer Program 2010*, CTR, Stanford, CA, USA, 405–422.